PAPER

Check for updates

Nanocage-based {SnEr$_2$}-organic framework for high catalytic performance in cycloaddition of CO$_2$ with epoxides and Knoevenagel condensation†

Xu Wang, [ID] *[a] BinBin Fan, [ID] [b] Jing Chen, [ID] [b] Jing Du[b] and Dahai Pan*[b]

The integration of abundant active sites and robust chemical stability in metal–organic frameworks (MOFs) is pivotal for advancing their industrial-scale utilization. This study proposes a novel strategy to construct cluster-based heterometallic MOFs by incorporating rare-earth ions. Through a solvothermal synthesis approach, we successfully engineered {[SnEr$_2$(HBDCP)(H$_2$O)]$_n$·3DFM·5H$_2$O}$_n$ (**TYUT-13**), a three-dimensional framework integrating Sn^{2+} (stannous(II) ions), Er^{3+} (erbium(III) ions) and designed flexible tetracarboxylic acid of 2,6-bis(2,4-dicarboxylphenyl)-4-(4-carboxylphenyl)pyridine (H$_5$BDCP). This architecture features a unique pore environment characterized by high porosity and dual-functional active sites (Lewis acidic Sn/Er centers and basic pyridinic N atoms), which synergistically enhance catalytic performance. Experimental results demonstrate that **TYUT-13a** exhibits exceptional activity in the solvent-free cycloaddition of CO$_2$ to epoxides under mild conditions (65 °C, 1 atm CO$_2$, 4 h), achieving >98% conversion efficiency. Furthermore, it displays broad applicability in Knoevenagel condensations between phenoxyacetaldehyde and malononitrile, with yields exceeding 97%. These findings highlight the effectiveness of rare-earth ion hybridization in balancing structural integrity and catalytic multifunctionality, offering a blueprint for designing next-generation MOF catalysts for sustainable chemical processes.

Introduction

Metal–Organic Frameworks (MOFs), as crystalline porous materials with modularly tunable architectures, have emerged as promising platforms for catalytic CO$_2$ cycloaddition toward carbon neutrality.[1–6] Their ultrahigh surface areas, precisely engineered pore geometries, and chemically tailorable active sites, enable efficient CO$_2$ capture and conversion.[7–9] However, conventional MOF catalysts suffer from critical limitations: (1) low active site density due to simplistic monometallic nodes and non-functionalized linkers, leading to compromised selectivity for bulky epoxides;[10–12] (2) restricted substrate diffusion in narrow micropores, causing kinetic bottlenecks despite high intrinsic activity;[13] (3) structural degradation under thermal or solvent exposure, resulting in rapid activity decay within 5 cycles.[14] To address these challenges, cutting-edge strategies—such as constructing bimetallic nodes for

synergistic catalysis, engineering hierarchical pores to balance selectivity and mass transport, and grafting hydrophobic ligands to enhance stability—are being actively pursued. These advancements, coupled with scalable synthesis techniques, position MOFs as next-generation catalysts for industrial carbon capture and utilization (CCU) systems.[15–18]

The unabated reliance on fossil fuels to meet surging global energy demands has precipitated unprecedented CO$_2$ emissions, exacerbating climate change and ecosystem degradation. This urgency has propelled CCU technologies to the forefront of sustainable research, aiming to reconcile energy security with environmental stewardship.[19,20] Paradoxically, while CO$_2$ is a prime driver of global warming, it simultaneously constitutes an underutilized C1 building block for synthesizing value-added products—from carbonates and methanol to biodegradable polymers—offering a dual solution to resource scarcity and emission mitigation.[21,22] However, the inherent thermodynamic stability of CO$_2$ imposes stringent activation requirements, compounded by its dilute concentrations in industrial flue gases. Such technical bottlenecks necessitate innovative materials that integrate selective adsorption with catalytic conversion under ambient conditions, thereby minimizing energy penalties. Within the CCU paradigm, the atom-economical cycloaddition of CO$_2$ with epoxides to form cyclic carbonates exemplifies a commercially viable pathway. These products serve as pivotal components in lithium-ion batteries, green solvents, and polycarbonate synthesis. Conventional

[a]School of Semiconductor and Physics, North University of China, Taiyuan, Shanxi, China. E-mail: 20150175@nuc.edu.cn

[b]College of Chemistry and Chemical Engineering, Taiyuan University of Technology, Taiyuan, Shanxi, China

catalytic platforms, including homogeneous organocatalysts and heterogeneous metal oxides, are hampered by inefficient mass transfer, catalyst leaching, or compromised activity under low CO_2 partial pressures. In contrast, MOFs, engineered with periodic nanostructures and coordinative versatility, have revolutionized this domain.[23–26] Their ultrahigh surface areas and modular functionality enable precise substrate orientation and cooperative activation of CO_2/epoxide substrates, achieving turnover frequencies (TOFs).

Motivated by these insights, we strategically designed a rare earth (RE)-based MOF system, leveraging the synergistic effects of erbium ions (Er^{3+}) and Sn^{2+} ions. The selection of Er^{3+} as primary nodes stems from their superior Lewis acidity compared to transition metals, which enhances substrate polarization in CO_2-involving reactions such as epoxide cyclo-addition and Knoevenagel condensation. To build a robust framework, 2,6-bis(2,4-dicarboxylphenyl)-4-(4-carboxylphenyl) pyridine (H_5BDCP) was employed as the organic linker, offering two critical advantages: hierarchical porosity engineering – five carboxylate groups and a rigid tripodal geometry enable the formation of interconnected mesopores ideal for gas diffusion and active site accessibility;[27] cluster-directed assembly – the bifurcated 2,4-dicarboxylphenyl arms facilitate coordination-driven aggregation of polynuclear [SnEr$_2$(HBDCP)(H$_2$O)] clusters, significantly lowering CO_2 adsorption activation energy.[28–30] Through solvothermal synthesis (DMF/H_2O, 120 °C, 72 h), we successfully constructed the hetero-metallic framework $\{[SnEr_2(HBDCP)(H_2O)]_n \cdot 3DFM \cdot 5H_2O\}_n$ (**TYUT-13**). These metrics position **TYUT-13** as a transformative candidate for industrial CCU applications, particularly in modular carbonate production systems requiring energy-efficient CO_2 valorization.

Experimental section

Synthesis of TYUT-13

TYUT-13 was synthesized *via* a solvothermal route: Er_2O_3 (37.80 mg, 0.10 mmol), $SnCl_2 \cdot 2H_2O$ (22.6 mg, 0.10 mmol), and H_5BDCP (55.70 mg, 0.10 mmol) were combined in an autoclave containing 6 mL of *N*,*N*-dimethylformamide (DMF) and 8 mL deionized H_2O. The mixture was acidified with 0.5 mL 0.5 M HNO_3 to modulate ligand deprotonation kinetics. Subsequently, the Teflon-lined reactor (25 mL capacity) was sealed and heated at 140 °C for 72 h under static conditions, followed by controlled cooling to ambient temperature (10 °C h^{-1} ramp rate). Purple block crystals were isolated by vacuum filtration, washed with anhydrous ethanol (3 × 5 mL), and air-dried, yielding 31% based on Er_2O_3. Elemental analysis (%) Calcd for $C_{56}H_{28}N_2O_{22}SnEr_2$: C 44.30, H 1.85, N 1.85; found: C 44.32, H 1.83, N 1.79. FT-IR (KBr pellet, cm^{-1}): 2827 (*vs.*), 2364 (w), 1604 (w), 1544 (m), 1400 (*vs.*), 1014 (*vs.*), 833 (w), 782 (m) (Fig. S1†).

Result and discussion

Crystal structural analysis

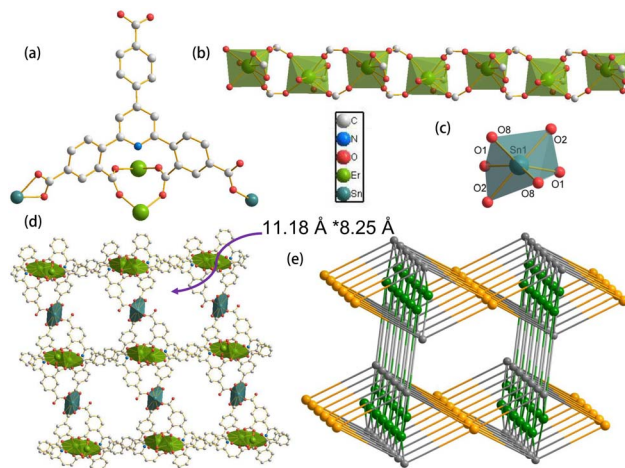Single-crystal X-ray diffraction analysis indicates that **TYUT-13** crystallizes within the triclinic system under the $P\bar{1}$ space group.

Fig. 1 Coordination pattern of the HBDCP^{4-} ligand (a), chain of {Er} (b), SBU of Sn (c), and three-dimensional sheet of **TYUT-13** (d), topology of **TYUT-13** (e).

As shown in Fig. 1a, the asymmetric unit comprises one Sn^{2+} center, two Er^{3+} ions, and a partially deprotonated HBDCP^{4-} ligand. In **TYUT-13**, the elaborate combination of $Sn(H_2O)^{2+}$ units, two $Er(H_2O)^{3+}$ units, and two deprotonated HBDCP^{4-} organic linkers generates a robust three-dimensional (3D) framework (Fig. 1d). This framework is stabilized by abundant hydrogen bonds arising from free carboxyl groups and coordinated water molecules. Notably, the 3D [SnEr$_2$(HBDCP)$_2$(H$_2$O)]$_n$ structure is functionalized by numerous free carboxyl groups, which function as Brønsted acid sites. Upon activation to remove coordinated water molecules, **TYUT-13a** emerges as a rarely documented host framework mediated by Lewis acid/Brønsted acid sites, establishing it as a promising multifunctional catalyst.

In **TYUT-13**, a typical six-coordinated Sn^{2+} is connected by four μ_2-η^1:η^1 carboxyl groups and one μ_2-OH group (Fig. 1c). The hepta-coordinated Er^{3+} in a pentagonal biconical polyhedron is constituted by one μ_1-η^1:η^1 γ-carboxyl group, four μ_2-η^1:η^1 carboxyl groups, and one μ_2-OH anion. Carboxyl groups from two phenyl rings located at the 2- and 6-positions of pyridine in a BDCP^{5-} moiety form binuclear [Er$_2$(CO$_2$)$_2$] units, which are further linked by a μ_2-OH group to produce a [Er$_2$(μ_2-OH)(CO$_2$)$_2$] unit. Significantly, all Er^{3+} ions are bonded through two μ_1-η^1:η^1 carboxylic acid linkages, extending into the 3D framework of **TYUT-13** (Fig. 1b). The Sn(Er)–O bond distances range from 2.127(9) to 2.360(10) Å, with O–Sn(or Er)–O angles spanning 48.2(5)° to 177.4(8)°. Moreover, the structural analysis of **TYUT-13** confirms that the orientation of H_5BDCP is due to the lone electron pair on pyridine N atoms, which strongly affects the two α-carboxyl groups on the 2,6-position benzene rings of pyridine to chelate metals with higher Lewis acidity. After chelating a metal ion, other carboxyl groups of H_5BDCP coordinate additional metal ions, resulting in the formation of binuclear or multinuclear metal-cluster nodes.

As for the topology, the host framework could be simplified as a {6^3}{6^3} network with HBDCP^{4-}, Er^{3+} and Sn^{2+} as 3-connected and 3-connected nodes, respectively, shown in Fig. 1e.

Gas adsorption studies

The IR spectrum indicates that the peak at 2827 cm^{-1} arises from the C–H bonds of alkyl groups. The peaks at 1604 cm^{-1} and 1544 cm^{-1} stem from the vibrations of the aromatic skeletal framework (C=C). The peak at 1014 cm^{-1} is associated with the vibrations of C–O bonds (Fig. S1†). The purity and water resistance of **TYUT-13** were characterized by powder X-ray diffraction (PXRD) analysis (Fig. S2†). The results show that the synthesized **TYUT-13** exhibits good stability, and its crystal structure remains intact even after being immersed in boiling water for 10 hours. The activated sample **TYUT-13a** was prepared through solvent exchange and thermal activation of the as-synthesized **TYUT-13** crystals. Specifically, residual guest molecules were removed *via* three cycles of anhydrous methanol immersion, followed by vacuum drying at 120 °C for 12 h to ensure complete pore activation. Thermogravimetric analysis (TGA) demonstrated robust framework stability with decomposition initiating at 360 °C (Fig. S3†). Nitrogen physisorption at 77 K revealed a type I isotherm (Fig. S4†), characteristic of microporous materials, with a Brunauer–Emmett–Teller (BET) surface area of 856 m^2 g^{-1} and Langmuir surface area of 974 m^2 g^{-1}. Furthermore, the aperture distribution measurement showed that its pore size ranged from 6.2 to 9.4 Å, which illustrates that there were inhomogeneous micro-porous channels in the framework. CO$_2$ adsorption capacities reached 128.6 cm^3 g^{-1} (273 K) and 65.4 cm^3 g^{-1} (298 K) at 1 bar (Fig. S5†), demonstrating temperature-dependent physisorption behavior. The isosteric heat of adsorption (Q_{st}) calculated *via* the Clausius–Clapeyron equation was 27.3 kJ mol^{-1} (Fig. S6†), consistent with weak physisorption interactions observed in most MOFs.[31-33] This value suggests that **TYUT-13a** achieves a balance between adsorption affinity and regeneration energy consumption, making it suitable for low-energy carbon capture applications. Subsequently, X-ray photoelectron spectroscopy (XPS) was employed to identify the diverse elements present in the **TYUT-13a** catalyst. The XPS survey spectrum, as presented in Fig. 2a, clearly reveals the existence of peaks corresponding to C 1s, N 1s, O 1s, Er 4d, and Sn 3d. In the C 1s XPS spectrum (Fig. 2b), the peaks at 284.8 eV, 285.4 eV, and 288.7 eV can be attributed to C–C/C=C, C–O/C–N, and C=O/C=N bonds, respectively. The N 1s XPS spectrum (Fig. 2c) confirms the
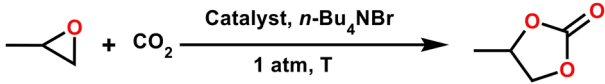
presence of N–N (402.0 eV) and N=N (399.3 eV) bonds. For the O 1s XPS spectrum (Fig. 2d), the peaks at 533.2 eV and 531.5 eV correspond to C–O and C=O bonds, respectively. Moreover, the Er 4d XPS spectrum (Fig. 2e) exhibits a peak at 169.2 eV (4d$_{5/2}$), indicating the presence of Er^{3+} in **TYUT-13a**. Additionally, the Sn 3d XPS spectrum (Fig. 2f), after deconvolution, yields two peaks at 486.9 eV (3d$_{5/2}$) and 495.3 eV (3d$_{3/2}$), which substantiate the existence of Sn^{2+} ions in **TUYT-13a**.[34,35]

Catalytic cycloaddition of CO$_2$ and epoxides

TYUT-13a, a bimetallic MOF integrating Sn^{2+}/Er^{3+} Lewis acid sites and HBDCP^{4-} ligand-derived Lewis base sites, demonstrated exceptional catalytic synergy for CO$_2$-epoxide cycloaddition. Initial trials under ambient conditions (25 °C, 1 atm CO$_2$) yielded minimal propylene carbonate (PC) production (only 2% in 24 h), highlighting the necessity of thermal activation (Table 1). Upon introducing 0.5 mol% *n*-Bu$_4$NBr as a co-catalyst, the PC yield surged to 99% at 65 °C within 24 h, attributed to Br$^-$ mediated epoxide ring-opening. Systematic optimization of reaction parameters identified 0.3 mol% **TYUT-13a** catalyst, 2.5 mol% TBAB co-catalyst, 65 °C, and 4 h as optimal conditions for the CO$_2$-epoxide cycloaddition. In addition, the efficiency of **TYUT-13a** catalyst in cycloaddition reaction is shown in Table S4.† It is worth noting that MOF outperforms most system catalysts in important parameters.[36-38]

The multifunctional catalyst **TYUT-13a**, engineered with synergistic Sn^{2+}/Er^{3+} Lewis acid sites and HBDCP^{4-} derived pyridinic N Lewis base motifs, achieves exceptional CO$_2$-epoxide

Table 1 Cycloaddition reaction of CO$_2$ with styrene oxide under various conditions^a

Entry	TYUT-13a (mol%)	*n*-Bu$_4$NBr (mol%)	Temp. (°C)	Time (h)	Yield^b (%)
1	0.10	0	25	24	2
2	0.10	0.5	25	24	44
3	0	0.5	25	24	20
4	0.10	0.5	35	24	59
5	0.10	0.5	45	24	76
6	0.10	0.5	55	24	85
7	0.10	0.5	65	24	97
8	0.10	1.0	65	22	97
9	0.10	1.5	65	20	98
10	0.10	2.0	65	18	98
11	0.10	2.5	65	16	97
12	0.15	2.5	65	12	98
13	0.20	2.5	65	9	98
14	0.25	2.5	65	6	99
15	0.30	2.5	65	4	99

^{a} Reaction conditions: 20 mmol ethylene oxide, solvent free, CO$_2$ (1 atm). ^{b} The *n*-dodecane was internal standard and checked by ^{1}H NMR.
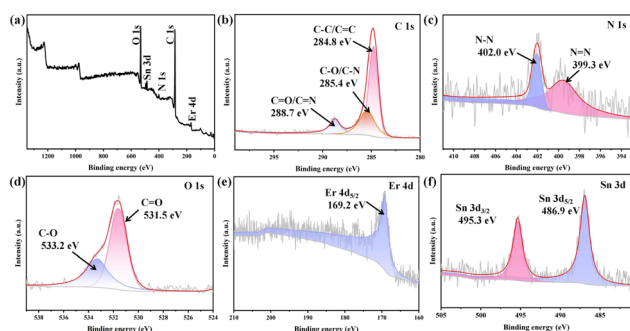

Fig. 2 (a) XPS survey spectra of **TYUT-13a**, (b–f) XPS spectra of C, N, O, Er and Sn, respectively, in **TYUT-13a**.
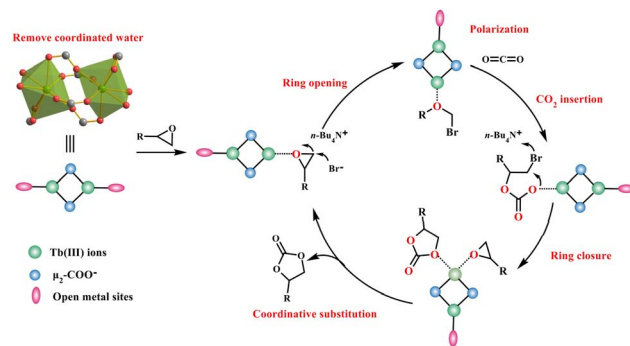
Table 2 The cycloaddition reactions of CO_2 with various epoxides with **TYUT-13a** as catalyst[a]

Entry	Epoxides	Products	Yield[b] (%)	TON[c]
1	(methyloxirane)	(product)	99	330
2	(F-epoxide)	(product)	100	333
3	(HO-epoxide)	(product)	97	323
4	(O-epoxide)	(product)	98	327
5	(vinyl epoxide)	(product)	98	327
6	(phenyl epoxide)	(product)	87	313

[a] Reaction conditions: substrates (20 mmol), n-Bu$_4$NBr (2.5 mol%), **TYUT-13a** catalyst (0.30 mol%), CO_2 (1 atm), 65 °C, 4 h. [b] The n-dodecane was internal standard and checked by GC-MS spectrometer. [c] TON(turnover number) = mole of product/mole of catalyst.

Fig. 3 The proposed reaction mechanism of catalytic coupling epoxides with CO_2.

cycloaddition performance under mild conditions (65 °C, 1 atm CO_2). Systematic substrate screening (Table 2) reveals near-quantitative conversion for small epoxides, as verified by ^{1}H NMR (Fig. S7–S11†), the decrease in yield for 2-phenyloxirane (Fig. S12†) can be attributed to the following: the tetracarboxylic acid linkers in **TYUT-13a** form a microporous framework with pore sizes of 6.2–9.4 Å. When 2-phenyloxirane approaches the Sn^{2+}/Er^{3+} Lewis acid sites, significant steric repulsion is encountered, which hinders effective coordination and C–O bond polarization. As reported in the literature on MOF-catalyzed cycloaddition reactions,[39–41] when the substrate size exceeds the pore diameter, reactivity decreases. Additionally, even with partial adsorption, the confined microporous channels impede mass transport of bulky molecules, creating kinetic bottlenecks.[42–44] The catalyst's superior efficiency over conventional MOFs arises from hierarchical activation: Er^{3+} (hard acid) and Sn^{2+} (soft acid) cooperatively polarize epoxides. This positions **TYUT-13a** as an excellent catalyst for CO_2 cycloaddition reactions.

The **TYUT-13a** catalyst exhibited exceptional cycling stability and structural integrity in the CO_2-epoxide cycloaddition reaction. Over five consecutive catalytic cycles (65 °C, 1 atm CO_2, 4 h per cycle), the catalyst retained 95% carbonate yield (Fig. S13†) after regeneration *via* centrifugation (6000 rpm), dichloromethane washing (3 × 10 mL), and vacuum drying (60 °C, 12 h), with 5% activity decay observed. Post-cycling PXRD patterns matched the activated sample (Fig. S14†), verifying preserved
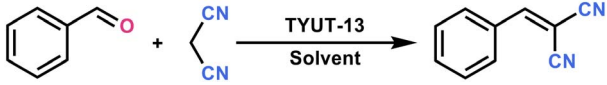
crystallinity without phase collapse or protonation-induced structural degradation. In addition, ICP analysis revealed that no Sn^{2+} ions were detected in the **TYUT-13**@Sn_2 suspension, indicating that the catalyst **TYUT-13a** maintained its structural stability after multiple cycles (Table S5†). Hot filtration tests at 65 °C revealed abrupt reaction termination at 64% conversion upon catalyst removal, with no further progress observed over 2 h (Fig. S15†), conclusively confirming heterogeneous catalysis.

Fig. 3 illustrates the proposed catalytic mechanism of **TYUT-13a** for the CO_2-epoxide cycloaddition. Step 1: the weakly coordinated Er^{3+} sites polarize the C–O bond of epichlorohydrin *via* Lewis acid–base interactions, activating the epoxide ring. Step 2: nucleophilic Br^- ions (released from N-Bu$_4$NBr) attack the β-carbon of the polarized epoxide, inducing ring-opening to form a bromoalkoxide intermediate. Step 3: CO_2 inserts into the Er^{3+} activated O–C bond, generating a linear alkyl carbonate species. Step 4: intramolecular cyclization occurs through carboxylate-assisted proton transfer, releasing the cyclic carbonate product while regenerating the catalytic sites. This dual activation mechanism combining Er^{3+} mediated epoxide polarization and Br^--driven nucleophilic attack-aligns with the cooperative catalysis observed in bimetallic MOFs.[45–50]

Catalytic activity of TYUT-13a on Knoevenagel condensation

Due to its rich active region, **TYUT-13a** exhibits excellent thermochemical stability at Er^{3+} and Sn^{2+} open metal sites, COOH acid sites, Lewis N and C=O base sites, which should conform to the main characteristics of bifunctional heterogeneous catalysts for organic reactions. Therefore, the catalytic properties of Knoevenagel condensation reaction were studied using phenoxyacetaldehyde (BDA, 10 mmol) and malononitrile (20 mmol) as model reagents and 1 mL dimethyl sulfide (DMSO) as the solvent. As shown in Table 3, the yield of 2-benzylnitrile (BDAN) product is 26% within 12 hours at 25 °C. The reaction was carried out using 0.10 mol% **TYUT-13a**. On the other hand, under the same conditions, conducting an empty experiment without **TYUT-13a** only detected trace amounts of BDAN (entry 2), indicating that **TYUT-13a** has certain catalytic activity for non-metallic condensation of Knoevenagel. Lewis bases N/C=O sites polarize the α-H of malononitrile *via* electrostatic interactions, lowering the activation energy for deprotonation.

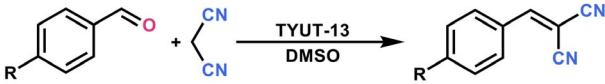**Table 3** Dagrammatic sketch of Knoevenagel condensation from substrates of BDA and malononitrile[a]

Entry	TYUT-13a (mol%)	Time (h)	Solvent	Temp. (°C)	Yield[b] (%)
1	0.10	12	DMSO	25	26
2	0	12	DMSO	25	3
3	0.10	12	CH_3CN	25	21
4	0.10	12	DMF	25	25
5	0.10	12	CH_3OH	25	22
6	0.10	12	C_2H_5OH	25	21
7	0.10	12	$C_4H_8O_2$	25	19
8	0.10	12	THF	25	17
9	0.10	12	Et_2O	25	13
10	0.10	12	C_6H_6	25	11
11	0.10	12	CHX	25	9
12	0.10	12	DMSO	35	42
13	0.10	12	DMSO	45	71
14	0.10	12	DMSO	55	94
15	0.15	11	DMSO	55	89
16	0.20	10	DMSO	55	90
17	0.25	9	DMSO	55	96
18	0.30	8	DMSO	55	95
19	0.35	7	DMSO	55	95
20	0.40	5	DMSO	55	97

[a] Reaction conditions: malononitrile (20 mmol), phenoxyacetaldehyde (10 mmol), solvent 1 mL. [b] The n-dodecane was internal standard and checked by GC-MS spectrometer.

Therefore, the effects of different reaction parameters such as solvent, reaction temperature, reaction time, and catalyst loading were studied. Next, as shown in entries 3–11, investigate the effects of different solvents on the reaction. Except for DMSO, the observed production coefficients correspond to the polarity of the solvents acetonitrile (CH_3CN), N,N-dimethylformamide (DMF), methanol (CH_3OH), ethanol (C_2H_5OH), 1,4-dioxins ($C_4H_8O_2$), tetrahydrofuran (THF), ether (ET_2O), benzene (C_6H_6), cyclohexane (CHX). Therefore, DMSO solvent is used for subsequent optimization. The conversion rate of BDA to BDAN significantly increases with the increase of reaction temperature, reaching 94% at 55 °C (entries 12–14). This is because as the reaction temperature increases, the collision frequency between substrate molecules and the active site of **TYUT-13a** increases, leading to an increase in macroscopic conversion rate. When the catalyst content reaches 0.40 mol%, the BDA matrix can be almost completely converted into BDAN products (entries 15–20). However, as the number of **TYUT-13a** increases, the reaction time no longer significantly shortens. Therefore, the optimal reaction conditions determined through the above experiments should be set as follows: 0.40 mol% **TYUT-13a** catalyst, reaction temperature of 55 °C, and reaction time of 5 hours. In addition, the efficiency of **TYUT-13a** catalyst in Knoevenagel condensation reaction is shown in Table S6.† It is worth noting that MOF outperforms most system catalysts in important parameters.[51–57]

Building upon **TYUT-13a** exceptional Knoevenagel performance, its catalytic versatility was further explored using substituted benzaldehydes with varied electronic and steric profiles. Under optimized conditions (0.40 mol% catalyst, 55 °C, DMSO), substrates bearing electron-withdrawing groups (–Br, –NO_2, –F) achieved quantitative conversion (Table 4, entries 1–3), as verified by ^{1}H NMR (Fig. S16–S21†). This enhancement arises from decreased aldehyde electron density, facilitating nucleophilic attack a trend reversed for electron-donating substituents (entries 4, 5: 89%, 81% yield). Steric hindrance significantly impacted reactivity: 4-(3,5-dimethylphenoxy)benzaldehyde showed 66% conversion at 5 h (entry 6), yet reached completion when prolonged to 11 h. These results validate **TYUT-13a** as a robust bifunctional catalyst, synergizing Er^{3+} mediated electrophile activation with Lewis base-assisted deprotonation.[58–61]

TYUT-13a demonstrated robust cycling stability in the Knoevenagel condensation reaction using benzaldehyde (BDA) as a model substrate under optimized conditions (0.40 mol% catalyst, 55 °C, DMSO). Over five consecutive cycles, the catalyst maintained 96% BDA conversion (Fig. S22†), with regeneration achieved via centrifugation (6000 rpm), dichloromethane washing (3 × 10 mL), and vacuum drying (60 °C, 12 h) to remove organic byproducts and preserve active sites. Post-reaction

Table 4 The Knoevenagel condensation reaction of aldehyde derivatives containing different groups[a]

Entry	Ester	Product	Yield[b] (%)	TON[c]
1			99	248
2			99	248
3			99	248
4			89	243
5			81	238
6			66	213

[a] Reaction condition: catalyst **TYUT-13a** (0.4 mol%), malononitrile (20 mmol), benzaldehyde dimethyl acetal derivatives (10 mmol), DMSO 1 mL, 55 °C, 5 h. [b] Calculation of yield based on GC and ^{1}H NMR. [c] TON (turnover number) = mole of product/mole of catalyst.
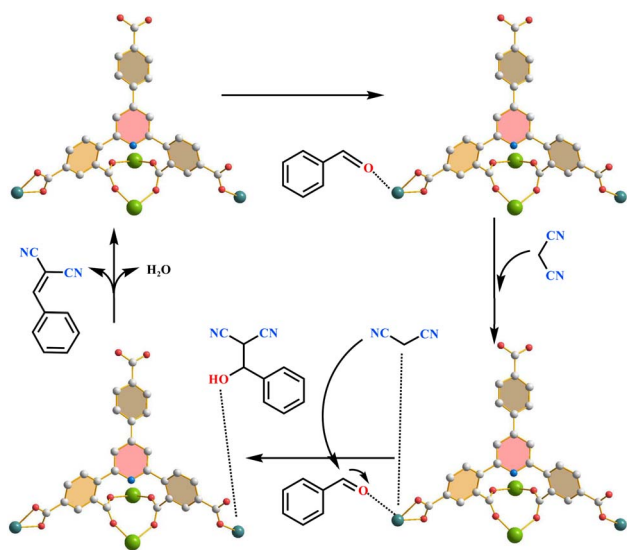
Fig. 4 The proposed reaction mechanism for Knoevenagel condensation.

PXRD patterns (Fig. S23†) exhibited identical characteristic peaks to the activated catalyst, indicating preserved crystallinity and chemical stability. Subsequent SEM-EDS characterization confirmed the structural integrity of **TYUT-13a** after cyclic reactions, revealing no detectable signs of framework degradation or elemental segregation (Fig. S24†). In addition, the ICP results showed that no Sn^{2+} ions were detected in the **TYUT-13@Sn_2** suspension, indicating that the catalyst **TYUT-13a** maintained its structural stability after multiple cycles of the Knoevenagel condensation reaction (Table S8†). Hot filtration experiments at 55 °C showed abrupt reaction termination (77% conversion) upon catalyst removal, with no further progress observed after 3 h of heating (Fig. S25†). These results position **TYUT-13a** as a high-performance catalyst for industrial Knoevenagel condensations.[62–64]

Based on current research, Fig. 4 shows the reaction mechanism of Knoevenagel condensation catalyzed by **TYUT-13a**, consisting of two reactions supported by Lewis acid and base. As the initial stage of the reaction, aldehyde oxygen atoms undergo COOH acid hydrolysis and polarize in a low distribution mode between Sn^{2+} and oxygen atoms to form electrophilic carbon atoms. As a Lewis base, the N atom then attracts the malonyl dinitro molecule to form hydrogen bonds, making the methacryloyl alcohol atom nucleophilic. Finally, dehydration leads to the formation of unsaturated olefins, and the **TYUT-13a** catalyst is released in the next catalyst cycle.[65–70]

Conclusions

The solvothermal self-assembly of Sn^{2+}, Er^{3+} and H_5BDCP led to the formation of an extremely stable microporous framework of $\{[SnEr_2(HBDCP)(H_2O)]_n \cdot 3DFM \cdot 5H_2O\}_n$ (**TYUT-13**) possessing an excellent confined pore environment with large specific surface area, high porosity, and abundant co-existing Lewis acid of Er^{3+}, Sn^{2+} and base sites of μ_2-OH and Npyridine atoms,

enabling exceptional catalytic performance in CO_2 cycloaddition (65 °C, 1 atm CO_2, 4 h) and Knoevenagel condensation (55 °C, 5 h) under mild conditions. Notably, **TYUT-13a** maintains structural integrity and activity over multiple cycles. This work highlights the critical role of high-coordination rare-earth ions in designing MOF catalysts with industrial-grade stability, catalytic efficiency, and recyclability.

Data availability

The authors confirm that the data supporting the findings of this study are available within the article and its ESI.†

Conflicts of interest

There are no conflicts to declare.

Acknowledgements

References

1 Q. Lv, Z. Zhu, S. Zhao, L. Wang, Q. Zhao, F. Li, L. A. Archer and J. Chen, *J. Am. Chem. Soc.*, 2021, **143**, 1941–1947.

2 J. Geng, Y. Ni, Z. Zhu, Q. Wu, S. Gao, W. Hua, S. Indris, J. Chen and F. Li, *J. Am. Chem. Soc.*, 2023, **145**, 1564–1571.

3 Y. Ni, L. Lin, Y. Shang, L. Luo, L. Wang, Y. Lu, Y. Li, Z. Yan, K. Zhang, F. Cheng and J. Chen, *Angew. Chem., Int. Ed.*, 2021, **60**, 16937–16941.

4 N. Seal, A. Karmakar, S. Kundu and S. Neogi, *ACS Sustainable Chem. Eng.*, 2023, **11**, 979–993.

5 Z. Luo, L. Liu, J. Ning, K. Lei, Y. Lu, F. Li and J. Chen, *Angew. Chem., Int. Ed.*, 2018, **57**, 9443–9446.

6 S. Zheng, D. Shi, D. Yan, Q. Wang, T. Sun, T. Ma, L. Li, D. He, Z. Tao and J. Chen, *Angew. Chem., Int. Ed.*, 2022, **61**, e202117511.

7 F. Wan, Z. Hao, S. Wang, Y. Ni, J. Zhu, Z. Tie, S. Bi, Z. Niu and J. Chen, *Adv. Mater.*, 2021, **33**, 2102701.

8 R. Abazari, N. Ghorbani, J. Shariati, R. S. Varma and J. Qian, *Inorg. Chem.*, 2024, **63**, 12667–12680.

9 M. Singh, A. Karmakar, N. Seal, P. Mondal, S. Kundu and S. Neogi, *ACS Appl. Mater. Interfaces*, 2023, **15**, 24504–24516.

10 L. Lin, Y. Ni, L. Shang, H. Sun, Q. Zhang, W. Zhang, Z. Yan, Q. Zhao and J. Chen, *ACS Catal.*, 2022, **12**, 7531–7540.

11 H. An, C. Li, Z. Lv, Y. Wang, H. Zhang, L. Zhao, R. Cheng, S. Wang, Q. Zhu, Z. Yin and D. Ma, *J. Phys. Chem. C*, 2023, **127**, 10515–10523.

12 K. Ohmatsu, R. Suzuki, H. Fujita and T. Ooi, *J. Org. Chem.*, 2023, **88**, 6553–6556.

13 K. Biradha, S. K. Das and X.-H. Bu, *Cryst. Growth Des.*, 2022, **22**, 2043–2045.

14 C. Han, X. Zhang, S. Huang, Y. Hu, Z. Yang, T.-T. Li, Q. Li and J. Qian, *Adv. Sci.*, 2023, **10**, 2300797.

15 J. Guo, D. Ma, F. Sun, G. Zhuang, Q. Wang, A. M. Al-Enizi, A. Nafady and S. Ma, *Sci. China Chem.*, 2022, **65**, 1704–1709.

16 X. Guan, Y. Qian, X. Zhang and H.-L. Jiang, *Angew. Chem., Int. Ed.*, 2023, **62**, e202306135.

17 R. Das, S. Kamraa and C. M. Nagaraja, *Inorg. Chem. Front.*, 2023, **10**, 2088–2099.

18 S. Liu, Y. Y. Sun, Y. P. Wu, Y. J. Wang, Q. Pi, S. Li, Y. Li and D. Li, *ACS Appl. Mater. Interfaces*, 2021, **13**, 26472–26481.

19 X. Yang, Y. Tian, S. Li, Y. Wu, Q. Zhang, D. Li and S. Zhang, *J. Mater. Chem. A*, 2022, **10**, 12225–12234.

20 N. Seal, A. Karmakar, S. Kundu and S. Neogi, *J. Mater. Chem. A*, 2024, **12**, 3501–3512.

21 C. Zhu, X. Zuo, W. Xian, Q. Guo, Q.-W. Meng, S. Wang, S. Ma and Q. Sun, *ACS Energy Lett.*, 2022, **7**, 2937–2943.

22 X. Liu, Y. Xie, M. Hao, Z. Chen, H. Yang, G. I. N. Waterhouse, S. Ma and X. Wang, *Adv. Sci.*, 2022, **9**, 2201735.

23 Y. Qian, Y. Han, X. Zhang, G. Yang, G. Zhang and H.-L. Jiang, *Nat. Commun.*, 2023, **14**, 3083.

24 M. Guo, Q. Meng, W. Chen, Z. Meng, M.-L. Gao, Q. Li, X. Duan and H.-L. Jiang, *Angew. Chem., Int. Ed.*, 2023, **62**, e202305212.

25 W. Han, X. Ma, J. Wang, F. Leng, C. Xie and H.-L. Jiang, *J. Am. Chem. Soc.*, 2023, **145**, 9665–9671.

26 L. Gong, Y. Liu, J. Ren, A. M. Al-Enizi, A. Nafady, Y. Ye, Z. Bao and S. Ma, *Nano Res.*, 2022, **15**, 7559–7564.

27 X. Wang, B. Li, Y. Wu, A. Tsamis, H. Yu, S. Liu, J. Zhao, Y. Li and D. Li, *Inorg. Chem.*, 2020, **59**, 4764–4771.

28 A. Nagaraj, R. Das and C. M. Nagaraja, *Microporous Mesoporous Mater.*, 2023, **351**, 112494.

29 R. Das, S. S. Manna, B. Pathak and C. M. Nagaraja, *ACS Appl. Mater. Interfaces*, 2022, **14**, 33285–33296.

30 J. Tian, Y. Wu, Y. Li, J. Wei, J. Yi, S. Li, J. Zhao and D. Li, *Inorg. Chem.*, 2019, **58**, 5837–5843.

31 Y. Song, C. Zhu and S. Ma, *Energy Chem.*, 2022, **4**, 100079.

32 M. Han, W. Zhang, L. Lu, S. Ma and S. Feng, *ACS Appl. Mater. Interfaces*, 2022, **14**, 28280–28288.

33 R. Das, V. Parihara and C. M. Nagaraja, *Inorg. Chem. Front.*, 2022, **9**, 2583–2593.

34 M. Jiang, P.-L. Zhao, Y.-N. Yue, X.-Q. Song and L. Wang, *J. Mol. Struct.*, 2024, **1316**, 138943.

35 J. Chen, J. Ma, Y. Ma, J. Luo, G. Cheng, W. Ran, Z. Liu, G. Wang, T. Tang, Z. Tang, M. Xu, L. Shen and Q. Wang, *J. Alloys Compd.*, 2025, **1022**, 180054.

36 L. Wen, K. Sun, X. Liu, W. Yang, L. Li and H.-L. Jiang, *Adv. Mater.*, 2023, **35**, 2210669.

37 J. Ding, X. Guan, J. Lv, X. Chen, Y. Zhang, H. Li, D. Zhang, S. Qiu, H. -L Jiang and Q. Fang, *J. Am. Chem. Soc.*, 2023, **145**, 3248–3254.

38 K. Sun, Y. Qian and H.-L. Jiang, *Angew. Chem., Int. Ed.*, 2023, **62**, e202217565.

39 R. Zhao, D. Chen, N. Gao, L. Yuan, W. Hu, F. Cui, Y. Tian, W. Shi, S. Ma and G. Zhu, *Adv. Funct. Mater.*, 2022, **32**, 2200618.

40 M. Singh, P. P. Mondal, S. Rajput and S. Neogi, *Chem. Front.*, 2023, **10**, 3605–3620.

41 H.-Q. Yin, M.-Y. Cui, H. Wang, Y.-Z. Peng, J. Chen, T.-B. Lu and Z.-M. Zhang, *Inorg. Chem.*, 2023, **62**, 13722–13730.

42 X. Zuo, C. Zhu, W. Xian, Q.-W. Meng, Q. Guo, X. Zhu, S. Wang, Y. Wang, S. Ma and Q. Sun, *Angew. Chem., Int. Ed.*, 2022, **61**, e202116910.

43 X. Liu, C. Zhu, J. Yin, J. Li, Z. Zhang, J. Li, F. Shui, Z. You, B. Shi, B. Li, X.-H. Bu, A. Nafady and S. Ma, *Nat. Commun.*, 2022, **13**, 2132.

44 J. Li, J.-Y. Huang, Y.-X. Meng, L. Li, L.-L. Zhang and H.-L. Jiang, *Chem. Commun.*, 2023, **59**, 2541–2559.

45 K. Qian, X. Guan, N. Sun and H.-L. Jiang, *Sci. China Chem.*, 2023, **66**, 436–442.

46 Y. Li, J. Sui, L.-S. Cui and H.-L. Jiang, *J. Am. Chem. Soc.*, 2023, **145**, 1359–1366.

47 J.-J. Zou, G. Wei, C. Xiong, Y. Yu, S. Li, L. Hu, S. Ma and J. Tian, *Sci. Adv.*, 2022, **8**, eabm4677.

48 Y. Ye, S. Xian, H. Cui, K. Tan, L. Gong, B. Liang, T. Pham, H. Pandey, R. Krishna, P. C. Lan, K. A. Forrest, B. Space, T. Thonhauser, J. Li and S. Ma, *J. Am. Chem. Soc.*, 2021, **144**, 1681–1689.

49 H. Wang, X. Liu, W. Yang, G. Mao, Z. Meng, Z. Wu and H.-L. Jiang, *J. Am. Chem. Soc.*, 2022, **144**, 22008–22017.

50 M.-L. Gao, L. Li, Z.-X. Sun, J.-R. Li and H.-L. Jiang, *Angew. Chem., Int. Ed.*, 2022, **61**, e202211216.

51 R. Das, T. Ezhil and C. M. Nagaraja, *Cryst. Growth Des.*, 2022, **22**, 598–607.

52 R. Dasa and C. M. Nagaraja, *Green Chem.*, 2021, **23**, 5195–5204.

53 C. Zhu, W. Xian, Y. Song, X. Zuo, Y. Wang, S. Ma and Q. Sun, *Adv. Funct. Mater.*, 2022, **32**, 2109210.

54 B. Ugale, S. S. Dhankhar and C. M. Nagaraja, *Cryst. Growth Des.*, 2018, **18**, 2432–2440.

55 P. Choudhary, A. Sen, A. Kumar, S. Dhingra, C. M. Nagaraja and V. Krishnan, *Mater. Chem. Front.*, 2021, **5**, 6265–6278.

56 L. Li, Y. Li, L. Jiao, X. Liu, Z. Ma, Y.-J. Zeng, X. Zheng and H.-L. Jiang, *J. Am. Chem. Soc.*, 2022, **144**, 17075–17085.

57 L.-L. Ling, L. Jiao, X. Liu, Y. Dong, W. Yang, H. Zhang, B. Ye, J. Chen and H.-L. Jiang, *Adv. Mater.*, 2022, **34**, 2205933.

58 W. Yang, X. Liu, X. Chen, Y. Cao, S. Cui, L. Jiao, C. Wu, C. Chen, D. Fu, I. D. Gates, Z. Gao and H.-L. Jiang, *Adv. Mater.*, 2022, **34**, 2270149.

59 Y. Pan, J. Wang, S. Chen, W. Yang, C. Ding, A. Waseem and H.-L. Jiang, *Chem. Sci.*, 2022, **13**, 6696–6703.

60 J. Sui, H. Liu, S. Hu, K. Sun, G. Wan, H. Zhou, X. Zheng and H.-L. Jiang, *Adv. Mater.*, 2022, **34**, 2109203.

61 X. Tian, X. Jiang, S. Hou, Z. Jiao, J. Han and B. Zhao, *Angew. Chem., Int. Ed.*, 2022, **61**, e202200123.

62 Z.-H. Zhu, B.-H. Zhao, S.-L. Hou, X.-L. Jiang, Z.-L. Liang, B. Zhang and B. Zhao, *Angew. Chem., Int. Ed.*, 2021, **60**, 23394–23402.

63 X. Jiang, Y. Jiao, S. Hou, L. Geng, H. Wang and B. Zhao, *Angew. Chem., Int. Ed.*, 2021, **60**, 20417–20423.

64 Y. Xie, Z.-H. Jiao, J. Dong, S.-L. Hou and B. Zhao, *Inorg. Chem.*, 2023, **62**, 5168–5175.

65 X.-R. Tian, Y. Shi, S.-L. Hou, Y. Ma and B. Zhao, *Inorg. Chem.*, 2021, **60**, 15383–15389.

66 J. Zhao, Z.-H. Jiao, S.-L. Hou, Y. Ma and B. Zhao, *ACS Appl. Mater. Interfaces*, 2021, **13**, 45558–45565.

67 Y.-H. Zou, Q.-J. Wu, Q. Yin, Y.-B. Huang and R. Cao, *Inorg. Chem.*, 2021, **60**, 2112–2116.

68 J. Li, Q. Yin, S.-Y. Gao, Y. Feng, S. Ye, H.-F. Li and R. Cao, *ACS Sustainable Chem. Eng.*, 2023, **11**, 4389–4397.

69 Z.-J. Lin, S. A. R. Mahammed, T.-F. Liu and R. Cao, *ACS Cent. Sci.*, 2022, **8**, 1589–1608.

70 W. Geng, X. Song, Z. Wei, M. Cao and R. Cao, *ACS Appl. Energy Mater.*, 2022, **5**, 15597–15604.